UNIVERSITY OF LEEDS

Article:
Koppal, S, Warntjes, M, Swann, J et al. (10 more authors) (2017) Quantitative fat and R2* mapping in vivo to measure lipid-rich necrotic core and intraplaque hemorrhage in carotid atherosclerosis. Magnetic Resonance in Medicine, 78 (1). pp. 285-296. ISSN 0740-3194

https://doi.org/10.1002/mrm.26359

Quantitative Fat and R2* Mapping *In-Vivo* to Measure Lipid-Rich Necrotic Core and Intraplaque Hemorrhage in Carotid Atherosclerosis

Sandeep Koppal[1,2], Marcel Warntjes[1,2,3], Jeremy Swann[4], Petter Dyverfeldt[1,2], Johan Kihlberg[1,5], Rodrigo Moreno[1,6], Derek Magee[4], Nicholas Roberts[7,8], Helene Zachrisson[1,2], Claes Forssell[9], Toste Länne[9], Darren Treanor[7,10], Ebo D de Muinck[1,2]

[1] Center for Medical Image Science and Visualization (CMIV), Linköping University, Linköping, Sweden
[2] Division of Cardiovascular Medicine, Department of Medical and Health Sciences, Linköping University, Linköping, Sweden
[3] SyntheticMR AB, Linköping, Sweden
[4] School of Computing, University of Leeds, United Kingdom
[5] Department of Radiology, Department of Medical and Health Sciences, Linköping University, Linköping, Sweden
[6] Current affiliation: KTH, Royal Institute of Technology, Stockholm, Sweden
[7] Department of Pathology and Tumor Biology, Leeds Institute of Molecular Medicine, University of Leeds, United Kingdom
[8] Current affiliation: Division of Brain Sciences, Department of Medicine, Institute of Neurology, Imperial College, London, United Kingdom
[9] Department of Thoracic and Vascular Surgery, and Department of Medical and Health Sciences, Linköping University, Linköping, Sweden
[10] Department of Clinical and Experimental Medicine, Linköping University, Linköping, Sweden

Word Count (body of the text): 4908

Running Title: Quantitative Mapping of Lipid Rich Necrotic Core and Intraplaque Hemorrhage

Corresponding Author:
E.D. de Muinck, MD, PhD, FAHA
Div. of Cardiovascular Medicine
Department of Medical and Health Sciences
Linköping University
SE-581 85 Linköping
Sweden
Tel. office: +46-10-1032112
Mobile phone: +46-730759843
ebo.de.muinck@liu.se

ABSTRACT

Purpose

To quantify the extent of lipid rich necrotic core (LRNC) and intraplaque hemorrhage (IPH) in atherosclerotic plaques.

Methods

Patients scheduled for carotid endarterectomy underwent four-point Dixon and T1-weighted magnetic resonance imaging (MRI) at 3T. Fat and R2* maps were generated from the Dixon sequence at the acquired spatial resolution of 0.60 x 0.60 x 0.70 mm voxel size. MRI and 3D histology volumes of the plaques were registered. The registration matrix was applied to segmentations denoting LRNC and IPH in 3D histology to split plaque volumes in regions with and without LRNC and IPH.

Results

Five patients were included. Regarding volumes of LRNC identified by 3D histology, the average fat fraction by MRI was significantly higher inside LRNC than outside: 12.64±0.2737 % versus 9.294±0.1762 % (mean±SEM, $P<0.001$). The same was true for IPH identified by 3D histology, R2* inside versus outside IPH was: 71.81±1.276 s^{-1} versus 56.94±0.9095 s^{-1} (mean±SEM, $P<0.001$). There was a strong correlation between the cumulative fat fraction by MRI and the volume of LRNC from 3D histology ($R^2=0.92$) as well as between cumulative R2* and IPH ($R^2=0.94$).

Conclusion

Quantitative mapping of fat and R2* from Dixon MRI reliably quantifies the extent of LRNC and IPH.

Key Words: magnetic resonance imaging; quantitative mapping; atherosclerosis; carotid artery.

INTRODUCTION

Decisions to intervene in atherosclerotic cardiovascular disease (CVD) are primarily based on stenosis severity. For example, patient selection for carotid endarterectomy (CEA) relies on the presence of symptoms indicative of cerebral ischemia and the degree of luminal narrowing caused by the carotid plaque (1). However, there is increasing evidence that stenosis severity alone is not sufficient to determine stroke risk. It has been shown that patients at high risk for stroke, but without any measurable stenosis, have a high proportion of advanced plaques (2). Furthermore, there is evidence that carotid plaque composition per se is a predictor of cardiovascular events (3). Thus, assessing carotid plaque composition non-invasively would arguably improve risk assessment for cardiovascular events, not only for stroke, but throughout the entire arterial circulation.

Plaques at high risk for causing arterial thrombosis with subsequent ischemic necrosis are called vulnerable plaques. Arterial thrombosis is most often caused by rupture or erosion of a vulnerable plaque (4). Established features of vulnerable plaques are lipid-rich necrotic core (LRNC), intraplaque hemorrhage (IPH), thin fibrous cap and, to a lesser extent, plaque calcification (4). Owing to its excellent soft tissue sensitivity, magnetic resonance imaging (MRI) has been used for carotid plaque characterization by multiple groups. Typically, blood suppressed T_1-weighted (T_1W), T_2-weighted (T_2W), proton density-weighted (PDW) fast spin echo, gradient echo and time of flight sequences are used (5). Using this multi-contrast approach, different plaque components can be identified, based on their relative signal intensity compared to the signal intensity of surrounding muscle, typically the sternocleidomastoid (6). Multi-contrast MRI has been successfully used to characterize carotid plaques, it has been validated by histology in a number of studies (5) and it offers stroke risk information beyond measurement of luminal narrowing in carotid atherosclerosis (7).

Despite these advantages, there are limitations to multi-contrast MRI of carotid plaque that prevent its wide-spread clinical application. One of these is that it relies on extensive post-acquisition assessment of differences in image intensity. The non-quantitative nature of this assessment, its operator dependency, its reliance on multiple sequences and the fact that the sequences are not entirely specific for the plaque components of interest, present barriers to the adoption of multi-contrast MRI in routine clinical practice. As mentioned above, for carotid

plaque imaging the sternocleidomastoid muscle is used as reference tissue. However, when the signal intensity form the adjacent muscle on fat- suppressed T_2W images is too low for use as a standard reference, the submandibular and parotid glands have been used (8). Ideally the reference tissue should represent a uniform distribution of intensity values, independent of its location within the image volume but in reality this is rarely the case. One of the biggest sources of intensity inhomogeneity is the surface coil used in carotid imaging and numerous approaches have been proposed to correct this problem (9). For example, all manufacturers use coil sensitivity maps acquired in separate reference scans to correct for intensity inhomogeneity, but because these maps only rescale to the homogeneity of integrated body coil, they do not necessarily provide a truly uniform homogeneity. Because of its proximity to the skin, intensity in images acquired from the sternocleidomastoid muscle is especially sensitive to the inhomogeneity caused by the sensitivity profile of surface coils. Thus, the issues with assessing plaque components based on relative image intensity emphasize the need for quantitative physical measurements of plaque constituents associated with vulnerability.

Regarding the validation of carotid plaque MRI, histology is the gold standard to determine plaque composition. Hence validation of *in vivo* MRI is possible by mapping histological data to *in vivo* data. Most often histology sections of the plaque are registered to *in vivo* images using the carotid bifurcation as a landmark (10). Due to the difference in MRI slice thickness (mm) and the thickness of histology sections (μm), there is a risk of inaccurate registration, even when using an easily recognizable landmark such as the carotid bifurcation. This problem increases with increasing distance from the bifurcation. The need for accurate registration of MRI and histology is further emphasized by the fact that there is significant variation in plaque composition along the length of the plaque (11). Adding to the complexity of registering 2D histology sections with MRI slices is the fact that out-of-plane angulations of the histology sections versus the MRI slices, as well as shrinkage and deformation during tissue processing are routinely neglected (12).

The goal of the current study was to develop a quantitative fat and R2* mapping technique to provide quantitative *in vivo* measurements of the extent of LRNC and IPH in carotid plaque. To this end we used a four-point Dixon gradient-echo sequence to measure LRNC and extracted the R2* value to quantify IPH. Originally proposed by Dixon (13), this gradient-echo sequence takes advantage of the slightly different resonance frequency of fat and water, which leads to

constructive and destructive interference of signal when measuring at different echo times. Analysis of the resulting signal oscillations allows for the calculation of the quantity of both water and fat in the human body (13). Simultaneously, signal is lost due to phase dispersion (the transverse T2* relaxation), which is increased by local magnetic field disturbances, for example due to the presence of iron. Therefore the rate of signal loss (R2* = 1/T2*) in a carotid plaque can be viewed as a measure for the presence of (heme) iron and thus can be expected to correlate to the extent of IPH. Indeed, in a different context, i.e. MRI of the brain R2* has been shown to correlate strongly and in a linear fashion with tissue iron content (14). Additionally, to overcome the shortcomings related to validation of *in vivo* MRI with 2D histology, we validated the MRI-based quantification of LRNC and IPH by correlating the measurements with registered 3D histology volumes of the plaques. A preliminary version of the current data was presented in poster format at the American Heart Association's Annual Scientific Sessions 2014 (15).

METHODS

The study was approved by Linköping's Institutional Review Board (record no.: 2012/321-32) and written informed consent was obtained from all participants prior to study entry.

Patients

Patients were included in the study if they were scheduled for CEA. The indication for CEA was the presence of a high grade (≥ 70%) carotid artery stenosis with or without recent (< 14 days) cerebrovascular ischemia in the form of stroke, transient ischemic attack or amaurosis fugax. Stenosis severity was assessed by measuring peak systolic velocity from the Doppler signal acquired during ultrasound imaging of the carotid artery, according to criteria established in the European Carotid Surgery Trial (16). All patients underwent MRI < 24 hours before surgery.

Magnetic Resonance Imaging

We applied a four-point Dixon sequence at 3T to generate high resolution maps of the fat percentage and values of R2* relaxation rate per voxel in atherosclerotic plaque. At 3T the 3.3 ppm frequency difference between water and fat creates an oscillating signal every 2.4 ms. Due to the limited gradient slew rate and strength needed to achieve sufficient resolution in the acquisition, we chose an out-of-phase, in-phase, out-of-phase, in-phase scheme, at echo times of

multiples of 3.6 ms (hence at TE = 3.6, 7.2, 10.8 and 14.4 ms). The water-fat-shift was maximized at 1.3 pixels. It was assumed that all voxels exhibited a single, effective R2* relaxation rate. Proton density and T1 relaxation differences between water and fat were not taken into account. Hence, the signal magnitude S at each echo time TE was modelled according to:

$$S(TE) = (W + Fcos(2\pi TE/2.4))\exp(-R2^{*}TE)$$

where W is the water fraction and F is the fat fraction. The water and fat percentages were calculated by division by the sum of the two. Other acquisition parameters for the sequence were TR = 18 ms, TFE factor 12 and flip angle 10 degrees. The field of view was 220x220x60 mm, centered on the flow divider at an isotropic acquisition resolution 0.75 mm, reconstructed at 0.60 mm. The acquisition used a Cartesian 3D read-out where k-space filling was performed from the center outwards (low-high, radial). The corners of k-space were not included, resulting in a cylindrical. Two regional saturation slabs of 80 mm were added inferior and superior to the acquisition volume, with a gap of 40 mm, to suppress inflowing blood signal. Using a TR = 18 ms and TFE = 12 these saturation bands were applied every 216 ms. The scan time was 9:45 minutes. Modelling and post-processing was performed in an adapted version of SyMRI software (SyntheticMR, Linköping, Sweden) producing fat, water and R2* maps at the acquired spatial resolution of 0.60 x 0.60 x 0.70 mm voxel size. The post-processing time was 10 seconds.

In addition to the four-point Dixon acquisition a T_1W TSE acquisition was performed with TE = 9 ms, TR = 1 heart-beat and TSE factor 6. A black-blood pulse sequence was used with a delay of 430 ms. The acquisition resolution was 0.55 mm, reconstructed at 0.47 mm; 18 slices of 2.1 mm, no gap, were acquired.

All scans were acquired on a 3T Philips Ingenia system using a 20 channel HeadNeckSpine coil (Philips Healthcare, Best, the Netherlands).

3D Histology and Image Registration

Figure 1 summarizes the tissue and image processing steps involved in the generation of the 3D histology volumes, image segmentation and registration. The plaques were fixed in 10% formalin immediately after surgery, decalcified, embedded in paraffin and trimmed at 50µm intervals. At every 50 µm step an image was taken of the plaque surface with the plaque

positioned vertically in the paraffin block. Thus, these so called *en face* images represent cross-sectional views of the plaque. An example is shown in the upper bar of Figure 1, to the right hand side of the caption "*En face* images from paraffin block". These images were taken using a fluorescent microscope with a mechanical stage using a 5x objective, taking advantage of the autofluorescence of the tissue (Imager.Z1 AxioCam MRm, Carl Zeiss, Jena, Germany). At every 200 µm step, a 5 µm thick section was taken for morphometric assessment of LRNC and IPH. Areas containing amorphous material and cholesterol crystals were classified as LRNC. The sections were stained trichrome to detect red blood cells and areas containing red blood cells were classified as IPH. Whole slide digital imaging of the stained sections was performed with brightfield microscopy using a 10x objective (Imager.Z1 AxioCam ERc 5s, Carl Zeiss, Jena, Germany).

The *en face* images were used to generate the 3D backbone for subsequent registration with the histology sections. To this end they were automatically registered to form a digital image stack using the StackReg plugin (17) within ImageJ 1.49 (National Institutes of Health, Bethesda, MD, USA). This image stack was loaded into ITK-SNAP 2.2 (Penn Image Computing and Science Laboratory (PICSL), University of Pennsylvania, Philadelphia, PA, USA), to automatically create a segmented volume using a sparse field level set segmentation method (18,19). Next, the stained histology sections were manually registered to the corresponding *en face* image within ImageJ using the interactive affine plugin, thus correcting for any deformations that might have occurred during sectioning and transfer onto the glass slide. The tissue expands when sectioned and transferred to the glass slide and to quantify the extent of expansion, morphometric analysis was used in ImageJ, measuring the area of the *en face* image in the paraffin block and the area of its corresponding trichrome stained section on the slide. A stack of the histology sections was then generated, imported into ITK-SNAP and 3D volumes of the LRNC and IPH were generated by manual segmentation. These volumes integrate the morphometric data on LRNC and IPH into the 3D backbone.

The resultant volumes and MRI data were imported into MeVisLab 2.2.1 (MeVis Medical Solutions AG, Bremen, Germany) where the T_1W MRI was automatically registered to the water, fat, and R2* maps from the four-point Dixon sequence using the MERIT framework within MeVisLab (20). The MRI data was up-sampled by a scale of 10 and the 3D histology volume was manually registered with the T_1W MRI by matching the lumen in the 3D histology

volume with the lumen within the MRI throughout the volume (Fig. 4A). The fresh sample shrinks during the processing steps that precede paraffin embedding and shrinkage was accounted for by manually stretching the 3D volume to match the lumen in the T_1W image thus achieving accurate registration of both volumes. To quantify the extent of shrinkage morphometric analysis was performed using ImageJ, comparing the area of the *en face* image with the area of the plaque on the cranial surface of the corresponding T_1W image slice. In addition this registration step allowed for adjustment of the 3D histology volume to out-of-plane angulations in the MRI (Fig. 4B). The resultant registration matrix was then applied to the segmentations denoting LRNC and IPH from 3D histology to split the plaque volume in regions with and without LRNC and IPH. For each of the resulting volumes (whole plaque, areas within LRNC, IPH and areas outside LRNC and IPH), the fat and R2* values in each voxel were recorded.

Statistical Analysis

Statistical analysis was performed using GraphPad Prism (version 6.05, GraphPad Software, Inc., La Jolla, CA, USA). An unpaired *t* test was used to analyze the differences between average MRI values per voxel within LRNC and IPH as defined by 3D histology versus the MRI values outside LRNC and IPH. These values are presented as a mean ±SEM and P-values < 0.05 were considered statistically significant. Linear regression analysis was performed to study the relationship between the cumulative value of corresponding MRI measurements from each voxel throughout the plaque and the volume of LRNC and IPH from histology. To assess the mean difference between the MRI values and the corresponding histological data and the 95% limits of agreement between them, Bland-Altman plots were generated. To account for the fact that the difference between the methods increased as the magnitude of the measured values increased, the approximate proportionality between difference and magnitude of the measurements was addressed as recommended by Bland and Altman, by plotting the ratio of the MRI values versus the 3D histology values as a function of their average (21).

RESULTS

Patients

A total of eight patients consented to participate in the study. In one patient the MRI was of insufficient quality due to bulk motion artefacts due to swallowing and in one patient the scan had to be aborted because of claustrophobia. Furthermore, in one patient the plaque specimen was too fragmented to be able to generate a 3D histology volume. Thus, here we report on five patients with good quality MRI and intact plaque specimens. In four patients the stenosis was associated with recent cerebral ischemia and in one patient the stenosis was asymptomatic. The clinical characteristics, cardiovascular risk factors, co-morbidity and medication of these patients are summarized in Table 1 and 2.

Registration of 3D Histology with Magnetic Resonance Imaging

All plaques exhibited LRNC and IPH and therefore were all classified as advanced lesions ranking in category VI of the American Heart Association's atherosclerotic lesion classification system (22). Registration of the histological sections to the 3D backbone showed that sectioning and positioning of the tissue on glass slides caused an expansion of the tissue by 15.4 ± 4.1 % (mean ± SD) relative to its dimensions in the paraffin block. The scaling factors used in registration of 3D histology to T_1W MRI are shown in Supporting Table 1. This registration revealed that average shrinkage of the plaque was 9.2 ± 2.1 % (mean ± SD) relative to the situation *in vivo*. The out-of-plane angulations in each patient are shown in Figure 4B which shows that there are clear differences between the scanning direction *in vivo* and the vertical orientation of the tissue section in the paraffin block.

Validation of Magnetic Resonance Imaging by 3D histology

After registration with 3D histology and segmentation of LRNC and IPH volumes based on the histology volumes, we were able to generate fat and R2* maps from Dixon imaging that gave us the fat fraction and R2* value for each voxel inside and outside the LRNC and IPH (Figs. 5, 6). Figure 7 illustrates the fat fractions and the R2* values throughout each individual plaque. As is apparent from this data, the extent of LRNC and IPH varied considerably between plaques and the MRI measurements tracked this variability. Because of the large variation in the extent of LRNC and IPH between plaques, we chose to use the same length for x and y axes but to vary the scale on these axes to reflect the different sizes of LRNC and IPH among plaques.

First, we compared the fat fractions and R2* values by MRI throughout all plaques inside and outside volumes of LRNC and IPH as identified by 3D histology. The average fat fraction by MRI was significantly higher inside LRNC than outside: 12.64±0.2737 % versus 9.294±0.1762 % (mean±SEM, $P<0.001$). The same was true for IPH identified by 3D histology, R2* was significantly higher inside IPH than outside: 71.81±1.276 s^{-1} versus 56.94±0.9095 s^{-1} (mean±SEM, $P<0.001$). As shown in Figure 6 these differences persisted at the same level of significance for each individual patient.

Next, we assessed the correlation between the cumulative fat fractions and R2* values from MRI and the volumes of LRNC and IPH from 3D histology. Taking together all values from all plaques, linear regression showed a strong correlation throughout all plaques between the cumulative fat fraction as measured in each voxel and the volume of LRNC from 3D histology ($R^2=0.92$) as well as between the cumulative R2* per voxel and the volume of IPH ($R^2=0.94$). These strong correlations were maintained at the level of the individual patient as shown in Figure 7. Figure 8 shows the mean difference and 95% limits of agreement between MRI and 3D histology. The cumulative fat fraction as measured by Dixon MRI and the volume of the LRNC are shown in Figure 6 which shows that for each plaque, there was a strong positive correlation throughout the plaque between the cumulative fat fraction by MRI and the LRNC volume from 3D histology. The correlation between cumulative R2* and the volume of IPH also showed strong positive correlations between these parameters for every plaque.

DISCUSSION

Here we show that plaque characteristics associated with a high risk of rupture and thrombosis, can be quantified *in vivo* at high resolution by MRI. Moreover, we use 3D histology to validate *in vivo* carotid MRI, thus increasing the reliability of histology based validation of *in vivo* vascular imaging.

Through registration of T_1W MRI with a four point Dixon gradient-echo sequence, we were able to accurately map the fat fraction and the R2* value of each voxel to atherosclerotic plaques in the internal carotid artery. There was high variability among the plaques regarding the extent of LRNC and IPH and the fact that we show strong correlations between MRI and 3D histology in all plaques speaks to the robustness and wide applicability of this technique.

As outlined earlier, a quantitative MRI method for the measurement of the extent of LRNC has not been available. Regarding IPH, others have assessed the extent of IPH using a T2 mapping technique (23). This technique was validated against multi contrast T_1W, PDW and T_2W carotid MRI but histological validation was not reported. Moreover, the T2 images were acquired using a spin-echo sequence, which precludes the acquisition of T2* and thus R2*. T2***** relaxation is seen only with gradient-echo imaging because transverse relaxation caused by magnetic field inhomogeneities is eliminated by the 180° pulse at spin-echo imaging (24). Importantly, the R2* value has a strong, linear correlation with tissue iron content. Using chemically determined iron concentrations, Langkammer et al. demonstrated that transverse relaxation rates show a strong, linear correlation with tissue iron concentration throughout the brain but that in white matter structures, only R2* showed a linear correlation with iron concentration (14). Thus, we chose R2* for the quantification of the extent of IPH. More recently quantitative T1 and T2 mapping has been proposed for plaque characterization but these sequences were not validated against plaque histology thus it remains to be determined which plaque components are identified by this technique (25).

Others have indicated the need for the validation of *in vivo* imaging using 3D histology and it has been used to optimize registration of carotid plaque histology to carotid MRI and CT angiography *in vivo* (12,26). The improvements in registration offered by 3D histology come from its ability to account for tissue deformation during different tissue processing steps as well as the angulation differences between the specimen positioned vertically in a paraffin block and the *in vivo* image. The need to correct for tissue deformation is emphasized by the degree of expansion that we were able to calculate after the tissue sections had been registered to the 3D backbone generated from the *en face* images of the specimen. Furthermore, we were able to correct for shrinkage of the fresh specimen by registering the 3D volume to *in vivo* MRI, using the vessel lumen as a landmark. This was greatly facilitated by the black blood sequence acquired during T_1W imaging, which, owing to its high signal to noise ratio, allowed for accurate delineation of the vessel lumen. Moreover, the ability of 3D histology to support correction of the registration errors caused by angulation differences between the paraffin embedded specimen plaque and *in vivo* MRI is illustrated by the fact that a small angulation error of 7° already results in a longitudinal displacement error of 0.6 mm (1 voxel) at a distance of 5 mm (12). The difficulties encountered in registration of 2D histology with 2D MRI slices are illustrated in

Figure 5 where we show that there is partial mismatch between 2D histology and 2D MRI because the difference in angulation between histology sections and MRI cannot be taken into account upon registration of 2D images. Importantly, here, we advance the utility of 3D histology beyond its ability to optimize registration by generating 3D volumes from the stack that include volumes relevant to the assessment of atherosclerotic plaque vulnerability, i.e. the volumes of LRNC and IPH. This enabled us to add a quantitative dimension to the improved registration offered by 3D histology by comparing the voxel-wise measurement of fat and R2* to the volume of LRNC and IPH upon 3D histology.

Multi-contrast MRI of carotid plaque has been used as a tool to assess stroke risk (7). However, to date it has been difficult to connect MRI biomarkers of carotid plaque vulnerability with the patho-biology of stroke and atherosclerotic plaque progression. There are numerous reasons for this lack of agreement between MRI and cerebrovascular ischemia as well as carotid plaque pathobiology. It cannot be ruled out however, that the lack of specificity for LRNC and IPH of the sequences currently used in multi-contrast plaque MRI, the non-quantitative nature of the approach and its operator dependency have a detrimental effect on accuracy and reproducibility in longitudinal studies. This, in turn, may impact the analysis of the relationship between patho-biology and imaging biomarkers of plaque instability. Here, we present a single sequence that allows for direct *in vivo* quantitative, automated mapping of LRNC and IPH in carotid plaque. Importantly, the method correlates closely with the extent of LRNC and IPH in 3D histology over a wide range of volumes of LRNC and IPH. Due to its quantitative nature, this approach may be able to improve estimation of stroke- and overall cardiovascular risk and elucidate the relationship between patho-biology and imaging biomarkers of plaque instability. Moreover, because of its relative simplicity and its use of automated voxel based quantification of LRNC and IPH it may prove to be particularly well suited for application in longitudinal studies.

A limitation inherent to the four-point Dixon method is its coarse modelling, where R2* differences, proton density differences and T1 relaxation differences between water and fat are ignored. Moreover, the fat frequency peak is known to consist of multiple components, with a broad width, leading to an effective increased relaxation rate. These model assumptions were made since adding more degrees of freedom to the analysis would not be valid for a four-point measurement. Our goal was to develop a sequence that would be practical in routine patient care,

thus a (relatively) short scan time and good repeatability for follow-up studies were important requirements. Therefore, we accepted a potential statistical offset for the water and fat fractions and other limitations inherent in the short scan time. Another limitation of our Dixon method is the T1-weighting due to the acquisition settings (TR = 18 ms, flip = 10 degrees). T1-weighting will suppress the water compartment more than the fat compartment, leading to an artificial enhancement of the fat content. This choice was made due to constraints regarding scan time and the signal to noise ratio (SNR). If the T1-weighting were to be limited to < 10% for both compartments a TR > 130 ms would be required, corresponding to a 7-fold increase in scan time. Since the exact T1-relaxation is unknown, no attempt was made to correct for this effect. It is therefore reasonable to assume that the T1 weighting in the current protocol will contribute to an overestimation of the fat content. An additional, related effect is the B1 inhomogeneity, which may cause differences in T1-weighting throughout the volume. This effect however, is expected to be small considering the size of the acquisition volume and the moderate effect of B1 differences on saturation differences. Furthermore, the additional signal loss due to susceptibility differences over the imaging volume was ignored, potentially leading to an underestimation of R2*. However, in view of the very high R2* values found in hemorrhagic plaques with rates of over 50 s^{-1}, the effect of susceptibility is expected to be negligible.

Regarding registration of 3D histology with MRI, it is to be expected that the strong correlations reported here between MRI based quantification of LRNC and IPH and 3D histology would be strengthened further if methods for non-rigid registration of MRI and 3D histology volumes had been available during the study. As expected there are slight differences in the slopes of the regression lines shown in Figure 7. In other words there is a strong correlation between the volume of LRNC and IPH and fat and R2* by MRI within each patient but there are differences between individual patients. This speaks to the strong heterogeneity in the composition of atherosclerotic plaques in general and the differences between patients in the current study. Even within areas designated as LRNC and IPH by their histological appearance, the tissue is heterogeneous (Fig. 3) and the fat and R2* values in one voxel may differ from those in adjacent voxels. Furthermore, there are sources of fat and blood outside the LRNC and IPH, in the form of lipid laden macrophage foam cells and capillaries that are filled with blood (3). We would submit however, that the strong correlations between 3D histology and MRI found for every patient speaks to the robustness of the MRI technique and that adequately

powered prospective studies will help establish threshold fat and R2* values that predict carotid plaque rupture and ischemic cerebral events.

Finally, image artifacts due to patient motion constitute a major issue in carotid MRI and around 15% of all carotid MRI scans have unacceptable image quality (27). In the current study the MRI quality was not compromised by motion artifacts in six out of seven patients in whom we were able to acquire MRI, thus our fail rate due to motion artifact is within the 15% reported by others. However, we acknowledge that our high-resolution Dixon sequence, scanned without a dedicated carotid coil has a relatively low SNR. In future studies we anticipate that the use of a dedicated carotid coil will increase the SNR and reduce the fail rate. Unfortunately, we did not have access to such a coil during the present study. The increased SNR could allow for reductions in scan time via the use of higher parallel imaging factors. In view of the long scan time and the small voxel size in the current imaging protocol, we would not use additional SNR to reduce voxel size. Furthermore, the present study did not use motion rejection techniques. Our 3D acquisition is relatively insensitive to pulsatile motion since the k-space read-out occurs in a radial low-high fashion. If a number of k-space lines display a different signal intensity due to blood flow for example the effect will, after Fourier Transform, be spread out as radial streaking artifacts over the entire image, and not, as in the linear Cartesian case as a band centered at the vessel. Bulk motion, however, disrupts the imaging, as exemplified in the one case that was excluded. Techniques that reject data acquired during swallowing such as free-induction decay navigators could be applied in the future to reduce the fail rate (28).

CONCLUSIONS

In conclusion, we present a quantitative mapping technique for atherosclerotic LRNC and IPH which relies on direct measurement of fat and iron sensitive imaging. Moreover, we have validated this technique thoroughly using 3D histology. The quantitative nature of this technique should facilitate the interrogation of the relationship between MRI biomarkers of carotid plaque vulnerability, atherosclerotic plaque progression and stroke from carotid plaque. Its reliance on a single sequence and the automated nature of the quantification should facilitate transferability between scanners and assessment of changes in LRNC and IPH in longitudinal studies.

SUPPORTING INFORMATION

Supporting Table 1. Scaling Factors Applied upon Registration of 3D Histology with Magnetic Resonance Imaging.

TABLES

Table 1. Baseline Characteristics

	Patient 1	Patient 2	Patient 3	Patient 4	Patient 5
Gender	male	female	female	male	male
Age (years)	64	75	79	66	90
Location of endarterectomy	right	left	left	right	left
Location of ≥ 70% stenosis	right	left	left	right	left
Symptomatic stenosis	yes	yes	yes	no	yes
Peak systolic flow velocity (m/sec.)	3.2	2.5	6.5	2.5	4.6
Stenosis severity	80-99%	70-79%	80-89%	70-79%	80-89%

Table 2. Cardiovascular Risk Factors, Co-Morbidity and Medication at Baseline

	Patient 1	Patient 2	Patient 3	Patient 4	Patient 5
Hypertension	yes	yes	yes	yes	yes
Body mass index (kg/m^2)	27	39	35	32	26
Total cholesterol (mmol/L)	3.3	4.4	4.6	3.0	4.8
LDL cholesterol (mmol/L)	1.2	2.3	2.8	1.2	n.a.
HDL cholesterol (mmol/L)	1.1	1.2	1.1	1.0	0.69
Triglycerides (mmol/L)	2.2	2.1	1.5	1.9	5.8
Diabetes mellitus	no	no	yes	yes	no
GFR (mL/min.)	112	94	54	72	65
Chronic kidney disease stage	1	1	1	1	2
Current smoker	yes	no	yes	no	no
Former smoker		no		yes	yes
Alcohol abuse	no	no	no	no	no
Other cardiovascular disease					
Ischemic heart disease	no	no	no	yes	yes
Lower extremity disease	no	no	yes	no	no
Atrial fibrillation	no	no	no	no	no
Heart failure	no	no	no	no	no
Medication					
Statin	yes	yes	yes	yes	yes
Platelet inhibitor	yes	yes	yes	yes	yes
Anti-coagulant	no	no	no	no	no
Anti-hypertensive	yes	yes	yes	yes	yes

GFR – glomerular filtration rate; HDL – high density lipoprotein; LDL – low density lipoprotein.

FIGURE LEGENDS

Figure 1. Segmentation and registration steps in 3D histology and registration with T_1-weighted magnetic resonance imaging.

Workflow outlining the steps involved and the software that was used in generating 3D histology volumes from carotid plaques obtained after carotid endarterectomy surgery. These volumes contain the volumes of lipid rich necrotic core and intraplaque hemorrhage and are subsequently registered to the corresponding T_1-weighted cardiovascular magnetic resonance image of the plaque.
ROI - region of interest.

Figure 2. Base magnetic resonance images for each patient.

For each patient, base images are shown for T_1W images, as well as fat, water and R2* maps from the Dixon sequence.

Figure 3. Histology of lipid rich necrotic core and intraplaque hemorrhage.

Trichrome stained histological section of carotid plaque showing regions of lipid rich necrotic core and intraplaque hemorrhage. The lipid rich necrotic core was identified as amorphous material containing cholesterol crystals and intraplaque hemorrhage was identified as contiguous areas containing red blood cells as visualized by the trichrome stain.

Figure 4. Registration of 3D histology and the corresponding T_1-weighted magnetic resonance image.

(A) The 3D histology volumes and MRI data from patient no. 1 are shown. The upper panels show non-zoomed T_1-weighted base images in the X, Y and Z direction. The fields of view for the zoom-ins are shown in red. The letters on the panels indicate the orientation of the images: A

= anterior, H = head, R = right. The middle panels show zoomed T_1W of the carotid artery lower panels in the X, Y and Z direction. The lower panels show the same images with the mask from 3D histology superimposed. The 3D histology and MRI volumes were manually registered in MeVisLab 2.2.1. (MeVis Medical Solutions AG, Bremen, Germany) by matching the lumen in the 3D histology volume with the lumen in the MRI. The scaling factors applied in all five patients during this registration to account for tissue shrinkage *ex-vivo* are shown in Supporting Table 1. (B) Range of angles showing the deviation from the vertical axis of the internal carotid artery in all patients as visualized from the T_1-weighted image. The lines deviating from the vertical axis indicate the path of blood flow through the internal carotid artery.
A – anterior; H- head; R – right.

Figure 5. Histology section, T_1-weighted image and corresponding fat and R2* maps showing clear separation of the fat fraction and R2* signal as well as limitations of registration of 2D histology with 2D magnetic resonance imaging slices.

Histology section and magnetic resonance imaging data showing the atherosclerotic plaque from patient no. 1. From left to right the panels show the histology section, the T_1-weighted image, and the corresponding fat and R2* maps of the atherosclerotic plaque (a-d). The plaque was segmented in the T_1W MRI after registration with 3D histology. The lower panels show the corresponding base MR images (e-g). The fields of view for the zoom-ins are shown in red. There is a clear separation of the highest fat fraction (white in (c) from the highest R2* value (white in (d). The area of lipid rich necrotic core from histology is indicated by the yellow line superimposed on panel (c) and the area of intraplaque hemorrhage is indicated by the red line superimposed on panel (d). In this patient the atherosclerotic plaque was at a 13.42° angle to the vertical plane (see Fig. 4B) resulting in a displacement error causing partial mismatch between 2D histology and 2D MRI as shown in the figure. An angulation error of 7° results in a displacement error of 0.6 mm (1 voxel) at a distance of 5 mm, thus here this error amounted to almost two voxels at 5 mm (12).

Figure 6. Average fat fractions and R2* values in- and outside lipid rich necrotic core and intraplaque hemorrhage.

Average fat fraction from Dixon imaging within regions of lipid rich necrotic core (labeled "In") as identified by 3D histology versus the average fat fraction in the rest of the plaque (labeled "Out") (a-e) and average R2* value from Dixon imaging within regions of intraplaque hemorrhage as identified by 3D histology versus the average R2* value in the rest of the plaque (f-j).
IPH – intraplaque haemorrhage; LRNC – lipid rich necrotic core; *** $P < 0.001$.

Figure 7. Correlation of cumulative fat fractions and R2* values with 3D histology.

The first column on the left shows visualization of the combined fat and R2* signal from Dixon imaging (a, e, i, m, q), where all masked tissue was depicted in 3D as transparent grey. The fat values were superimposed with a yellow linear color ramp using a threshold of 5%. The R2* values were superimposed with a red linear color ramp using a threshold of $50s^{-1}$. The red arrows show the orientation of the internal carotid artery from which the plaque was retrieved. The next column directly to the right shows 3D histology volume renderings of the atherosclerotic plaque (b, f, j, n, r). The orientation is identical to the internal carotid artery visualized from magnetic resonance imaging. The lipid rich necrotic core volume is indicated in yellow and the intraplaque hemorrhage volume is indicated in red. The next two columns show correlation plots of the cumulative fat fraction (c, g, k, o, s) and the cumulative R2* value (d, h, l, p, t) within the plaque from the Dixon sequence against the volume of the lipid rich necrotic core and intraplaque hemorrhage from 3D histology.
IPH – intraplaque hemorrhage; LRNC – lipid rich necrotic core.

Figure 8. Bland-Altman plots showing the mean difference and the 95% limits of agreement between magnetic resonance imaging and 3D histology.

Bland-Altman plots showing the mean difference and 95% limits of agreement for the two methods. The upper row (a-e) shows the mean difference and 95% limits of agreement for cumulative fat fraction from Dixon imaging and the volume of lipid rich necrotic core from 3D histology. The lower row shows the same for the cumulative R2* value and the volume of intraplaque hemorrhage (f-j). As is apparent from Figure 7, the difference between the methods increases as the magnitude of the measured values increases. As recommended by Bland and Altman, this approximate proportionality between difference and magnitude of the measurements was addressed by plotting the ratio of the MRI values versus the 3D histology values as a function of their average (21).
IPH – intraplaque hemorrhage; LRNC – lipid rich necrotic core.

REFERENCES

1. Kernan WN, Ovbiagele B, Black HR, et al. On behalf of the American Heart Association Stroke Council, Council on Cardiovascular and Stroke Nursing, Council on Clinical Cardiology, and Council on Peripheral Vascular Disease. Guidelines for the prevention of stroke in patients with stroke and transient ischemic attack: a guideline for healthcare professionals from the American Heart Association/American Stroke Association. Stroke 2014;45:2160-2236.
2. Dong L, Underhill HR, Yu W, Ota H, Hatsukami TS, Gao TL, Zhang Z, Oikawa M, Zhao X, Yuan C. Geometric and compositional appearance of atheroma in an angiographically normal carotid artery in patients with atherosclerosis. AJNR Am J Neuroradiol 2010;31:311-316.
3. Hellings WE, Peeters W, Moll FL, et al. Composition of carotid atherosclerotic plaque is associated with cardiovascular outcome: a prognostic study. Circulation 2010;121:1941-1950.
4. Naghavi M, Libby P, Falk E, et al. From vulnerable plaque to vulnerable patient: a call for new definitions and risk assessment strategies: Part I. Circulation 2003;108:1664-1672.
5. den Hartog AG, Bovens SM, Koning W, Hendrikse J, Luijten PR, Moll FL, Pasterkamp G, de Borst GJ. Current status of clinical magnetic resonance imaging for plaque characterisation in patients with carotid artery stenosis. Eur J Vasc Endovasc Surg 2013;45:7-21.
6. Saam T, Ferguson MS, Yarnykh VL, Takaya N, Xu D, Polissar NL, Hatsukami TS, Yuan C. Quantitative evaluation of carotid plaque composition by in vivo MRI. Arterioscler Thromb Vasc Biol 2005;25:234-239.
7. Gupta A, Baradaran H, Schweitzer AD, Kamel H, Pandya A, Delgado D, Dunning A, Mushlin AI, Sanelli PC. Carotid plaque MRI and stroke risk: a systematic review and meta-analysis. Stroke 2013;44:3071-3077.
8. Watanabe Y, Nagayama M. MR plaque imaging of the carotid artery. Neuroradiology 2010;52:253-274.
9. Salvado O, Hillenbrand C, Zhang S, Wilson DL. Method to correct intensity inhomogeneity in MR images for atherosclerosis characterization. IEEE transactions on medical imaging 2006;25:539-552.
10. Yuan C, Mitsumori LM, Ferguson MS, Polissar NL, Echelard D, Ortiz G, Small R, Davies JW, Kerwin WS, Hatsukami TS. In vivo accuracy of multispectral magnetic resonance imaging for identifying lipid-rich necrotic cores and intraplaque hemorrhage in advanced human carotid plaques. Circulation 2001;104:2051-2056.
11. Lovett JK, Gallagher PJ, Rothwell PM. Reproducibility of histological assessment of carotid plaque: implications for studies of carotid imaging. Cerebrovasc Dis 2004;18:117-123.
12. Groen HC, van Walsum T, Rozie S, et al. Three-dimensional registration of histology of human atherosclerotic carotid plaques to in-vivo imaging. J Biomech 2010;43:2087-2092.
13. Dixon WT. Simple proton spectroscopic imaging. Radiology 1984;153:189-194.
14. Langkammer C, Krebs N, Goessler W, Scheurer E, Ebner F, Yen K, Fazekas F, Ropele S. Quantitative MR imaging of brain iron: a postmortem validation study. Radiology 2010;257:455-462.
15. Koppal S, Warntjes M, Swann J, Dyverfeldt P, Kihlberg J, Moreno R, Magee D, Roberts N, Treanor D, de Muinck ED. Direct in vivo Quantification of Intraplaque Hemorrhage and Fat in Atherosclerosis by Magnetic Resonance Imaging. 2014 Nov. 15-19, 2014; Chicago, IL, USA. Circulation. p A20143.
16. Randomised trial of endarterectomy for recently symptomatic carotid stenosis: final results of the MRC European Carotid Surgery Trial (ECST). Lancet 1998;351:1379-1387.

17. Thevenaz P, Ruttimann UE, Unser M. A pyramid approach to subpixel registration based on intensity. IEEE transactions on image processing : a publication of the IEEE Signal Processing Society 1998;7:27-41.
18. Yushkevich PA, Piven J, Hazlett HC, Smith RG, Ho S, Gee JC, Gerig G. User-guided 3D active contour segmentation of anatomical structures: significantly improved efficiency and reliability. NeuroImage 2006;31:1116-1128.
19. Whitaker RT. A Level-Set Approach to 3D Reconstruction from Range Data. International Journal of Computer Vision 1998;29:203-231.
20. Boehler T, van Straaten D, Wirtz S, Peitgen HO. A robust and extendible framework for medical image registration focused on rapid clinical application deployment. Computers in biology and medicine 2011;41:340-349.
21. Bland JM, Altman DG. Measuring agreement in method comparison studies. Stat Methods Med Res 1999;8:135-160.
22. Stary HC. Natural history and histological classification of atherosclerotic lesions: an update. Arterioscler Thromb Vasc Biol 2000;20:1177-1178.
23. Biasiolli L, Lindsay AC, Chai JT, Choudhury RP, Robson MD. In-vivo quantitative T2 mapping of carotid arteries in atherosclerotic patients: segmentation and T2 measurement of plaque components. J Cardiovasc Magn Reson 2013;15:69.
24. Chavhan GB, Babyn PS, Thomas B, Shroff MM, Haacke EM. Principles, techniques, and applications of T2*-based MR imaging and its special applications. Radiographics 2009;29:1433-1449.
25. Coolen BF, Poot DH, Liem MI, Smits LP, Gao S, Kotek G, Klein S, Nederveen AJ. Three-dimensional quantitative T1 and T2 mapping of the carotid artery: Sequence design and in vivo feasibility. Magn Reson Med 2016;75:1008-1017.
26. van Engelen A, Niessen WJ, Klein S, Groen HC, Verhagen HJ, Wentzel JJ, van der Lugt A, de Bruijne M. Atherosclerotic plaque component segmentation in combined carotid MRI and CTA data incorporating class label uncertainty. PLoS One 2014;9:e94840.
27. Boussel L, Arora S, Rapp J, Rutt B, Huston J, Parker D, Yuan C, Bassiouny H, Saloner D; MAPP Investigators. Atherosclerotic plaque progression in carotid arteries: monitoring with high-spatial-resolution MR imaging--multicenter trial. Radiology 2009;252:789-796.
28. Dyverfeldt P, Deshpande VS, Kober T, Krueger G, Saloner D. Reduction of motion artifacts in carotid MRI using free-induction decay navigators. J Magn Reson Imaging 2014;40:214-220.

Figure 1.

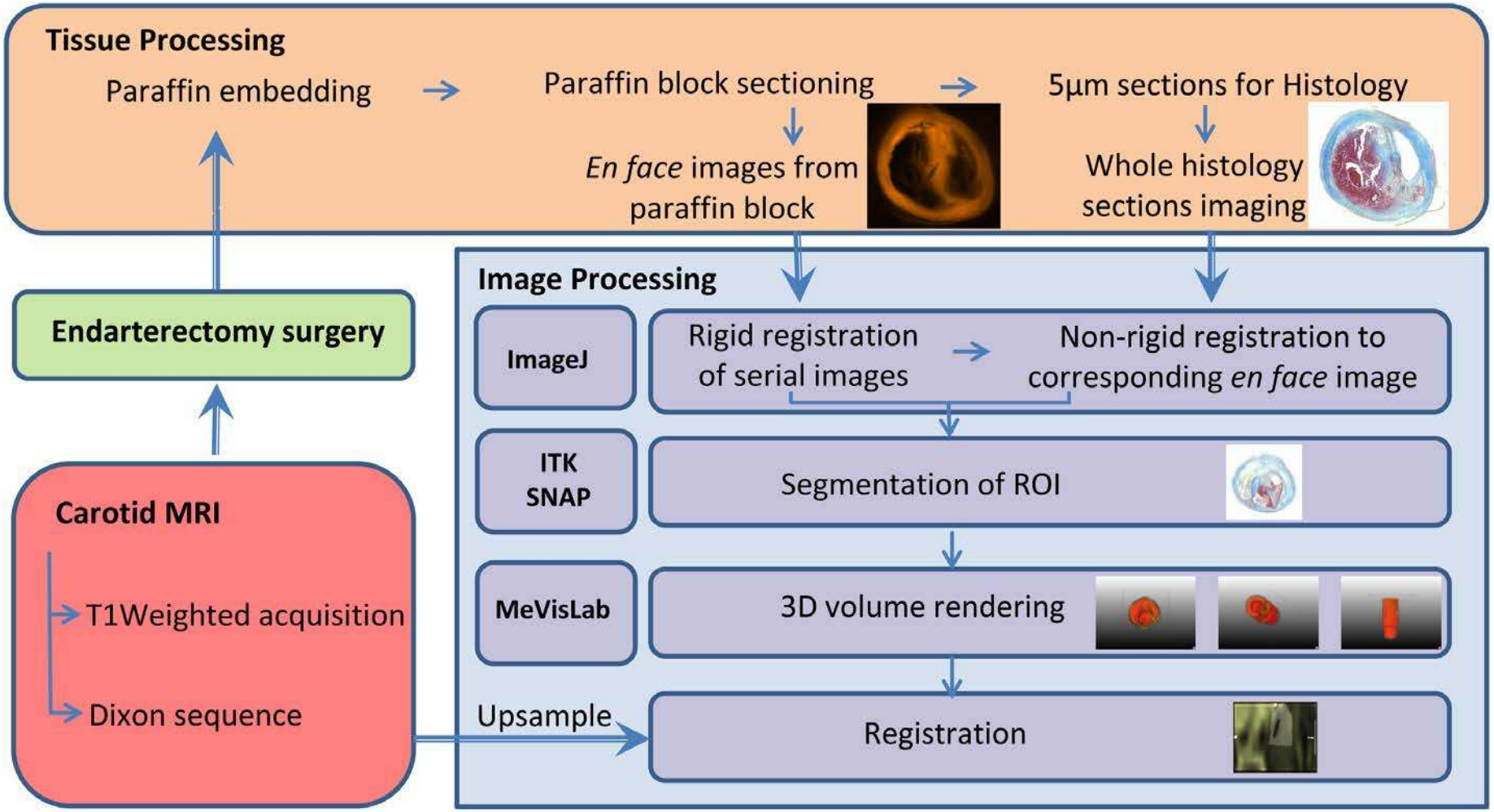
Tissue Processing
Paraffin embedding
Paraffin block sectioning
5µm sections for Histology
En face images from paraffin block
Whole histology sections imaging
Endarterectomy surgery
Image Processing
ImageJ
Rigid registration of serial images
Non-rigid registration to corresponding en face image
ITK SNAP
Segmentation of ROI
Carotid MRI
T1Weighted acquisition
Dixon sequence
MeVisLab
3D volume rendering
Upsample
Registration

Figure 2.

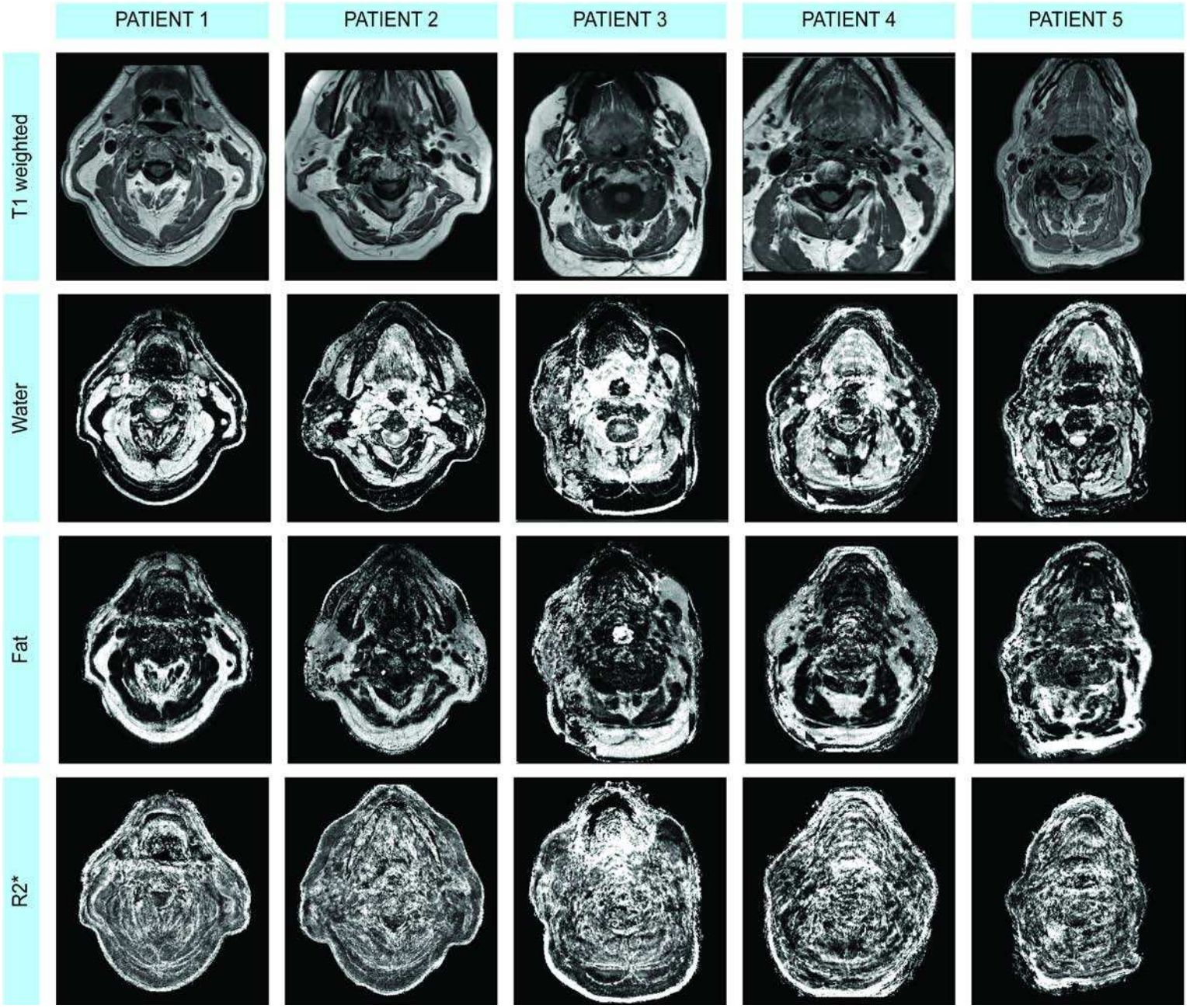
PATIENT 1
PATIENT 2
PATIENT 3
PATIENT 4
PATIENT 5
T1 weighted
Water
Fat
R2*

Figure 3.

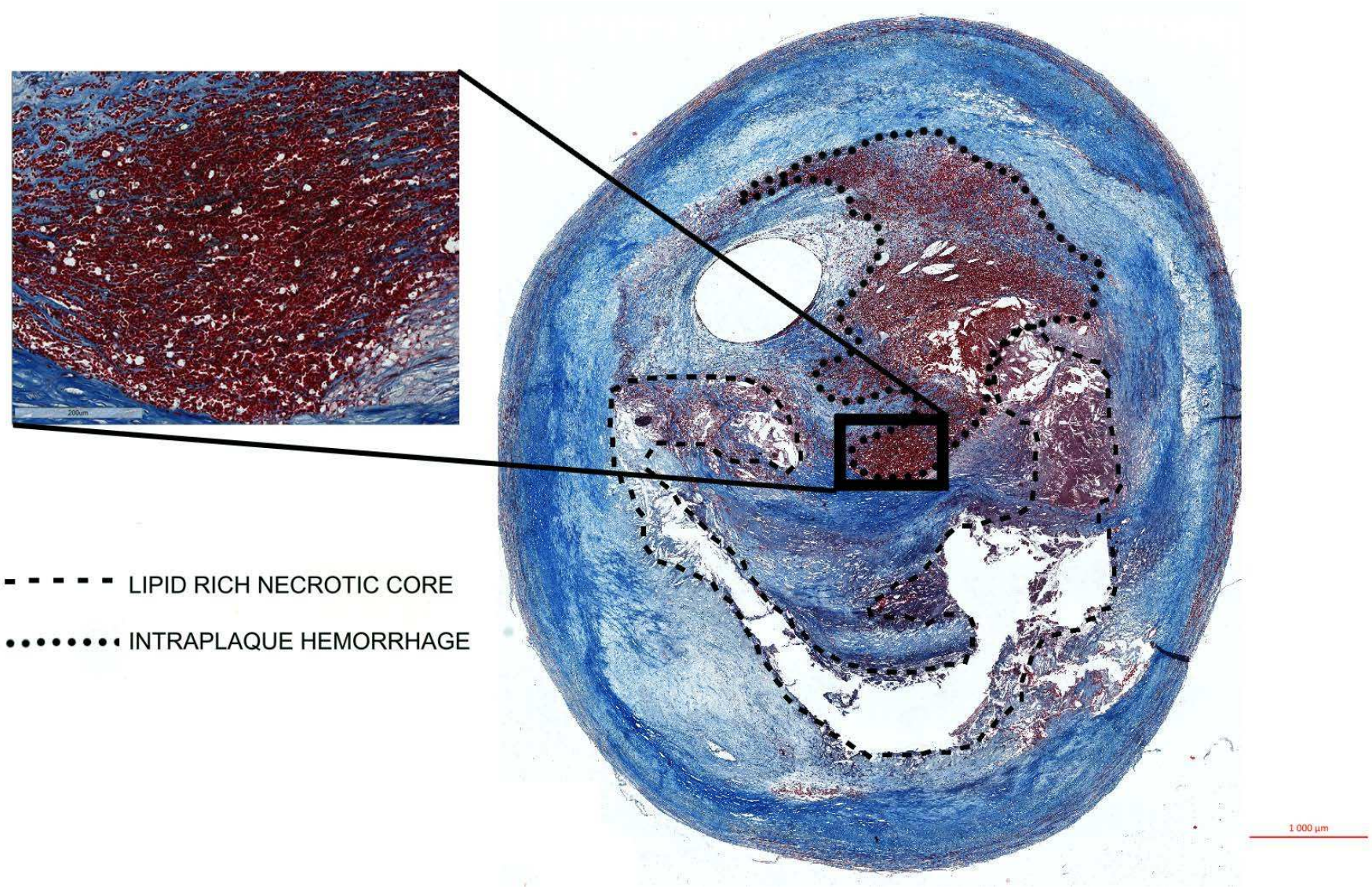

Figure 4.

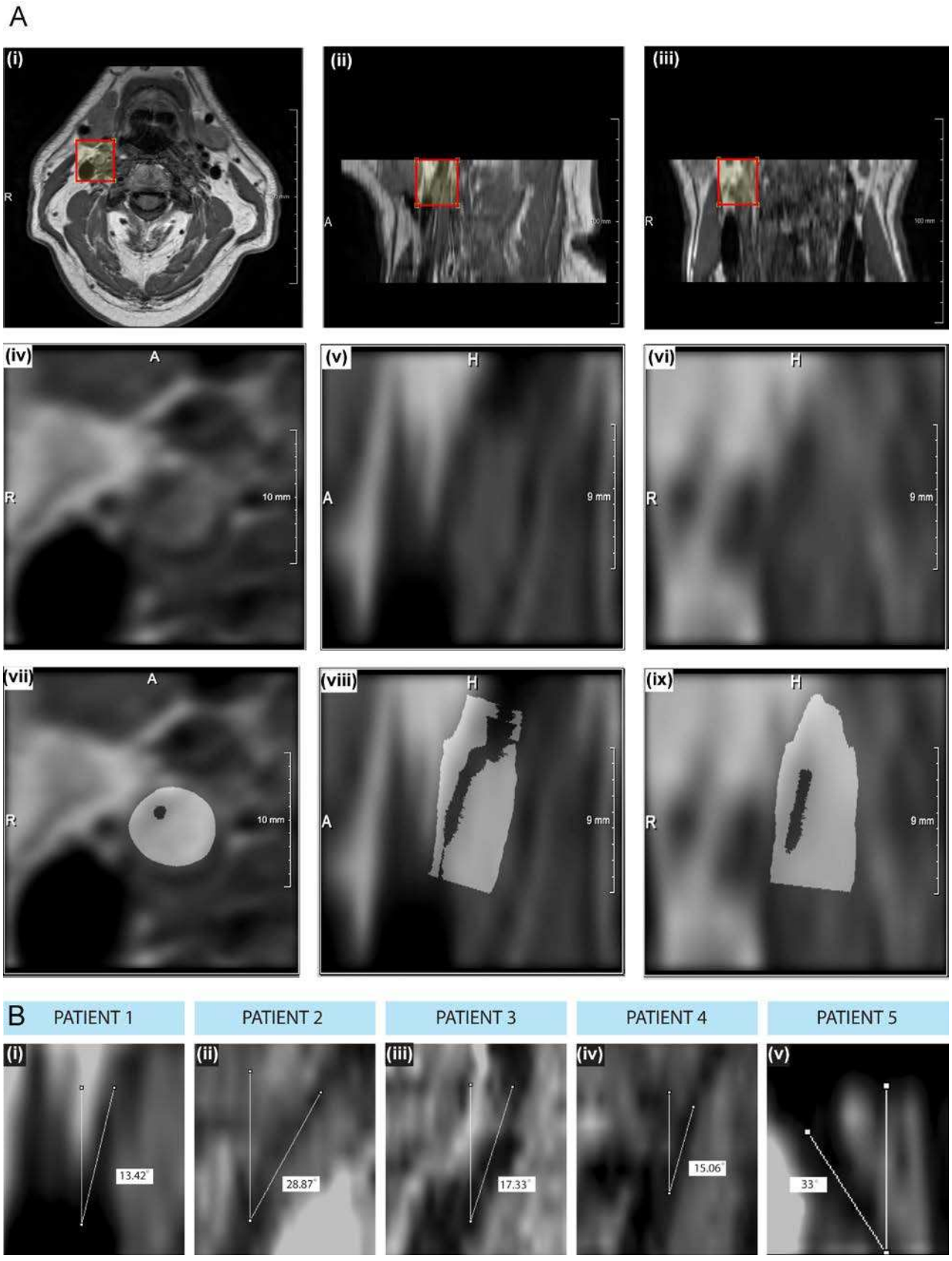
A
(i)
(ii)
(iii)
(iv)
(v)
(vi)
(vii)
(viii)
(ix)
R
A
H
10 mm
9 mm
B
PATIENT 1
PATIENT 2
PATIENT 3
PATIENT 4
PATIENT 5
13.42°
28.87°
17.33°
15.06°
33°

Figure 5.

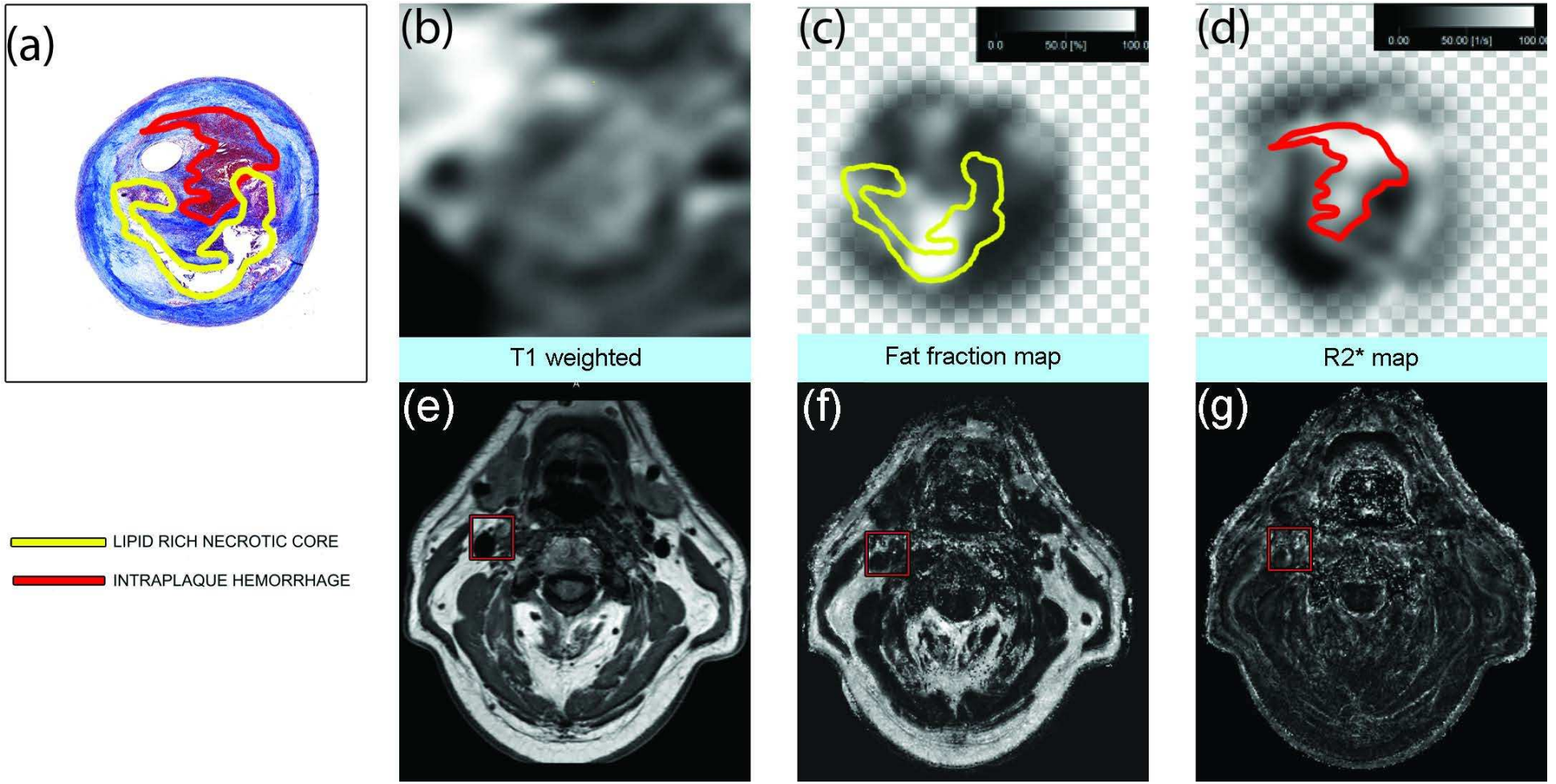
(a)
(b)
(c)
(d)
T1 weighted
Fat fraction map
R2* map
(e)
(f)
(g)
LIPID RICH NECROTIC CORE
INTRAPLAQUE HEMORRHAGE

Figure 6.

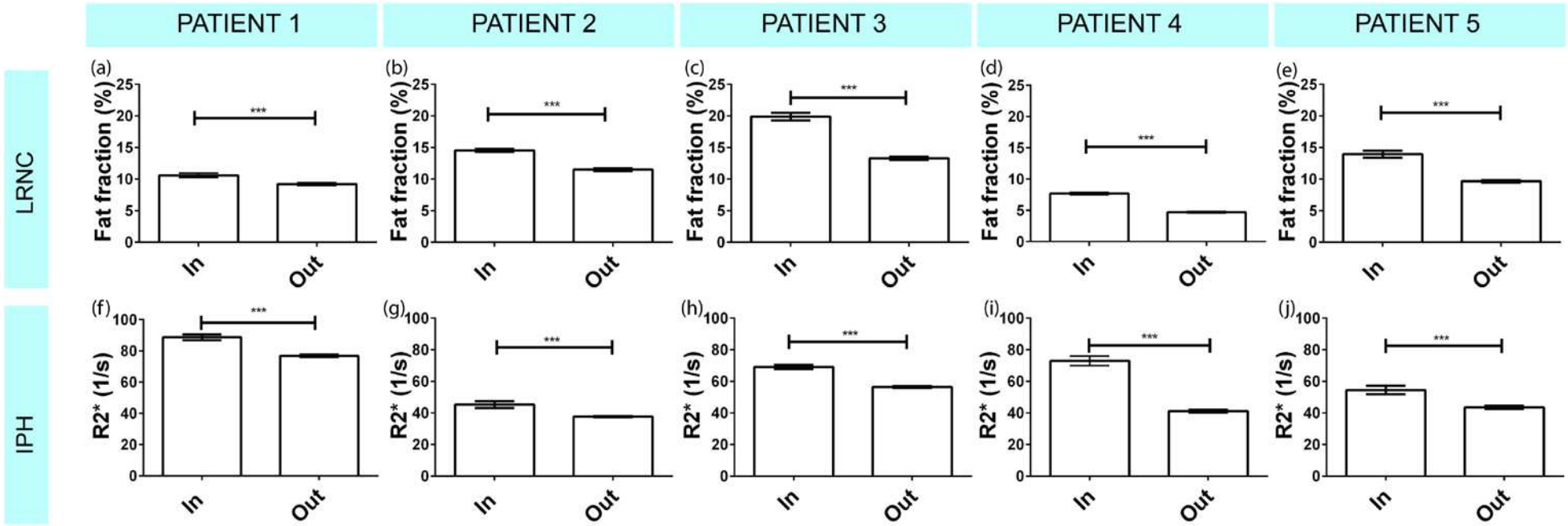
PATIENT 1
PATIENT 2
PATIENT 3
PATIENT 4
PATIENT 5
LRNC
IPH
(a)
(b)
(c)
(d)
(e)
(f)
(g)
(h)
(i)
(j)
Fat fraction (%)
R2* (1/s)
***
In
Out

Figure 7.

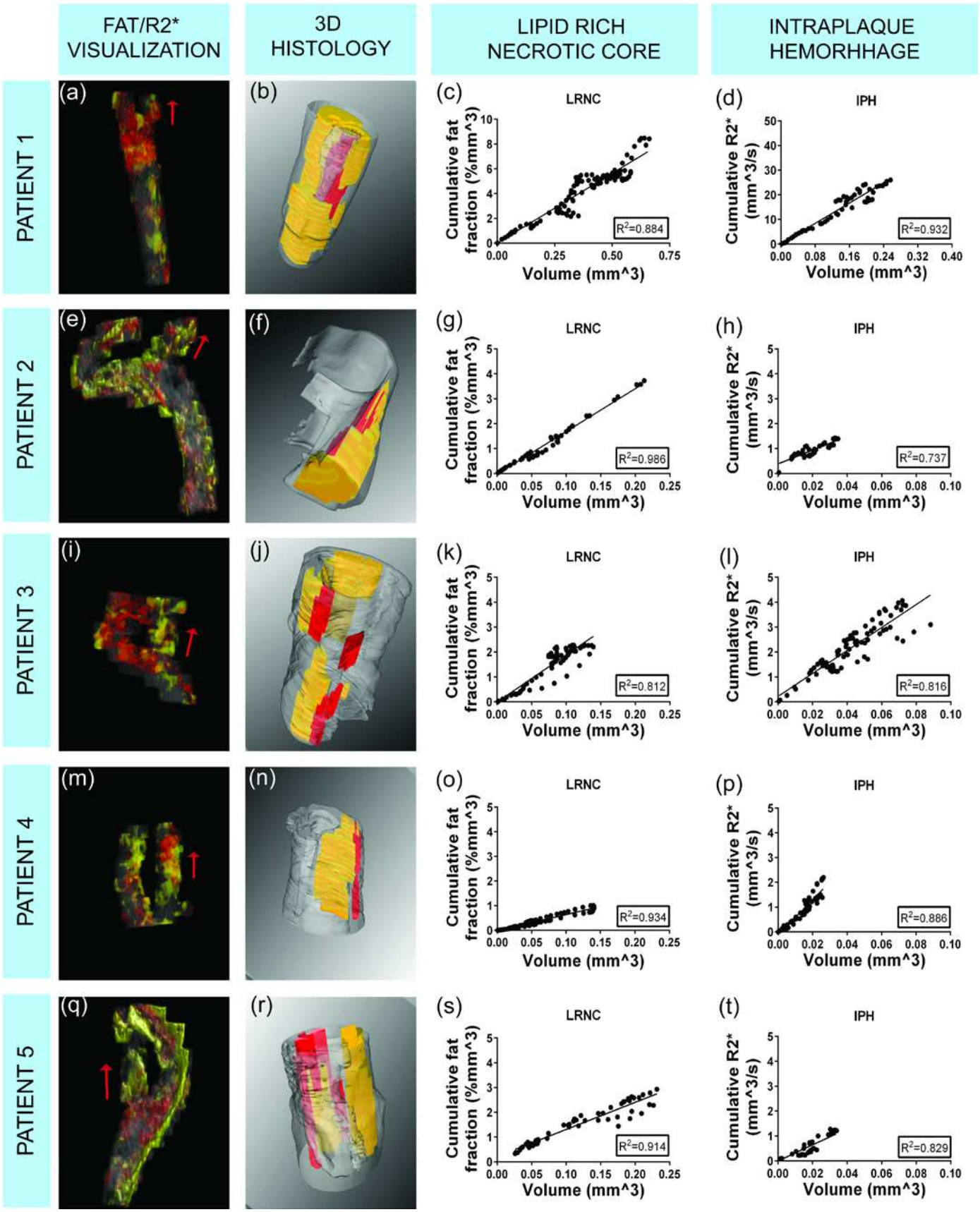
FAT/R2* VISUALIZATION
3D HISTOLOGY
LIPID RICH NECROTIC CORE
INTRAPLAQUE HEMORRHAGE
PATIENT 1
PATIENT 2
PATIENT 3
PATIENT 4
PATIENT 5
(a)
(b)
(c)
LRNC
Cumulative fat fraction (%mm^3)
Volume (mm^3)
R²=0.884
(d)
IPH
Cumulative R2* (mm^3/s)
R²=0.932
(e)
(f)
(g)
R²=0.986
(h)
R²=0.737
(i)
(j)
(k)
R²=0.812
(l)
R²=0.816
(m)
(n)
(o)
R²=0.934
(p)
R²=0.886
(q)
(r)
(s)
R²=0.914
(t)
R²=0.829

Figure 8.

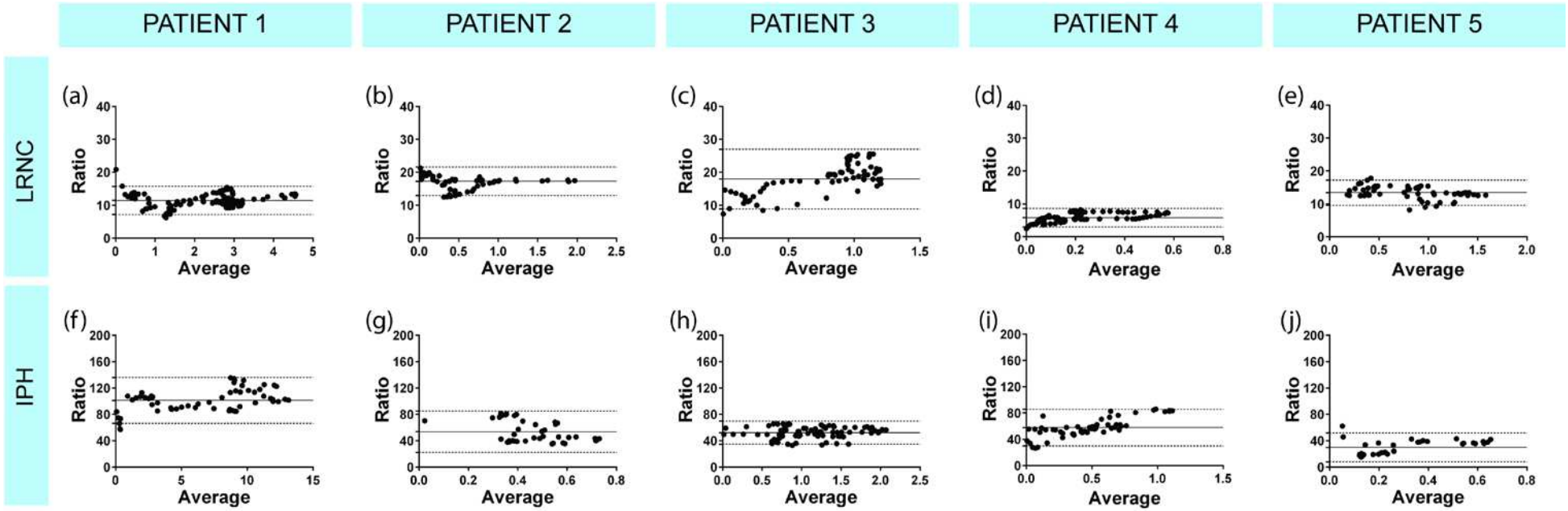

$$Ratio = \frac{\text{Cumulative MRI signal}}{3D\ histology\ volume}$$

$$Average = \frac{\text{Cumulative MRI signal} + 3D\ histology\ volume}{2}$$

SUPPORTING INFORMATION

Supporting Table 1. Scaling Factors Applied upon Registration of 3D Histology with Magnetic Resonance Imaging.

	X	Y	Z
Patient 1	0.021	0.021	0.06
Patient 2	0.021	0.021	0.06
Patient 3	0.021	0.021	0.06
Patient 4	0.0207	0.0207	0.06
Patient 5	0.0203	0.0203	0.06

The 3D histology volumes and MRI data were manually registered in MeVisLab 2.2.1. (MeVis Medical Solutions AG, Bremen, Germany) by matching the lumen in the 3D histology volume with the lumen in the MRI. The table shows the scaling factors applied in all five patients during this registration to account for tissue shrinkage *ex-vivo*.